

Available online at www.sciencedirect.com

jmr&t
Journal of Materials Research and Technology
journal homepage: www.elsevier.com/locate/jmrt



Original Article

Unravelling thermal-mechanical effects on microstructure evolution under superplastic forming conditions in a near alpha titanium alloy



Tabassam Yasmeen ^a, Salaheddin Rahimi ^a, Christopher Hopper ^b,
Chi Zhang ^b, Jun Jiang ^{b,*}

^a Advanced Forming Research Centre (AFRC), University of Strathclyde, 85 Inchinnan Drive, Inchinnan, PA4 9LJ, UK

^b Department of Mechanical Engineering, Imperial College London, London, UK

ARTICLE INFO

Article history:

Received 18 January 2022

Accepted 12 April 2022

Available online 18 April 2022

Keywords:

Superplastic forming

Dynamic crystallization

Microstructure evolution

Dislocation

ABSTRACT

The superplastic formability of titanium alloys has been extensively exploited by various industries, especially for manufacturing of high value aerospace components. Material's microstructural characteristics, such as grain size and dislocations density, determine superplastic formability during manufacturing process and various constitutive relationships have been proposed to take their effects into consideration in modelling and simulation. However, most existing models do not include all these characteristics in their analyses due to the limitations in characterization techniques. This paper reports the results of a systematic study on the effects of thermal (i.e., static) and mechanical (i.e., dynamic) process parameters on the evolution of dislocations and microstructure, both independently and simultaneously, at superplastic forming regime. The evolution of microstructural phase fraction, grain size, crystallographic texture, and geometrically necessary dislocation (GND) density are investigated over a temperature range of 880–920 °C and under strain rates between 0.0005 and 0.01s⁻¹. The results provide valuable insights into the microstructure evolution during superplastic forming on TA15 titanium alloy and form a basis for future physically based constitutive modelling.

© 2022 The Authors. Published by Elsevier B.V. This is an open access article under the CC BY license (<http://creativecommons.org/licenses/by/4.0/>).

1. Introduction

Titanium alloys are widely used in the manufacture of various aerospace components with complex geometries by superplastic forming (SPF) due to their combination of high strength-to-weight ratio, corrosion resistance and thermal

stability under severe operation conditions [1–3]. Recently, the increased utilization of composite materials in aerospace industry has further stimulated the demand for titanium alloys. This is due to the high compatibility of titanium alloys with composites due to their relatively low galvanic corrosion rate and superior mechanical strength in comparison to other rival aerospace alloys e.g., aluminum. For instance, an

* Corresponding author.

E-mail address: jun.jiang@imperial.ac.uk (J. Jiang).

<https://doi.org/10.1016/j.jmrt.2022.04.063>

2238-7854/© 2022 The Authors. Published by Elsevier B.V. This is an open access article under the CC BY license (<http://creativecommons.org/licenses/by/4.0/>).

increase in composite usage from 11% in Boeing 777 (i.e., launched in 1994) to 50% in Boeing 787 (i.e., launched in 2009) led to an increase in titanium usage from 7% to 15%, respectively. Similarly, titanium usage in military aircrafts is even more intense, as for example titanium alloys occupy 42% of F-22 Raptor fighter body structure materials, mainly for the manufacture of the wings, fuselage, skins, and load-bearing parts.

The structural integrity of superplastically formed parts made from titanium alloys can be significantly affected by the material microstructure, particularly when there is a change in geometry *e.g.*, drastic heterogeneity in wall thickness. Consequently, the microstructure of the formed parts is vital for their in-service performance such as fatigue resistance. Thus, understanding microstructure evolution during their manufacturing processes is critically important. Until now, no comprehensive study has been conducted on the manufacturing processes to understand the relationships between the dynamic loading as a function of strain, strain rate and temperature, and their combined effects on microstructure evolution. Although there are some studies on microstructure evolution in titanium alloys during superplastic deformation [4–7], the effects of dynamic loading on microstructure evolution are obscured by the complex effects of static thermal annealing that occurs concurrently. A study performed by Motyka et al. [8] shows that superplastic deformation of Ti–6Al–4V alloy at 875 °C/0.001s⁻¹ led to a decrease in the volume fraction of β -phase in both grip and gauge zones of the specimen, although the effect was greater in the gauge region. On the other hand, during superplastic deformation of a Ti3Al based alloy under testing conditions of 850 °C/0.0005 s⁻¹, as investigated by Yang et al. [9], the volume fraction of the β -phase in the grip sections was found to be higher than that of the gauge region, but only limited data was obtained. A study on an aluminum alloy deformed at 550 °C/0.0002 s⁻¹ by Friedman and Ghosh [10], found grain size to increase faster during superplastic deformation than that during static annealing alone. Similarly, Kaibyshev et al. [11] found a considerably higher grain growth in gauge regions compared to grip regions for an aluminum alloy deformed under strain rate of 0.0028 s⁻¹ at temperature range of 500–580 °C. For a magnesium alloy, Cao et al. [12] reported that in both grip and gauge regions, grain size increased linearly with decreasing strain rate and increasing temperature, with the effect being more pronounced in the grip regions. Similarly, other studies [13–16] reported smaller grain sizes in gauge regions as compared to grip regions. In summary, it is clear from the literature review that most studies consider only one microstructure parameter, i.e., grain size, for a comparative analysis of microstructure evolution under static annealing and superplastic forming conditions. There is no comprehensive study to date which uses a consistent framework considering multiple microstructural attributes (i.e., phase change, grain size, grain orientation, texture, and geometrically necessary dislocations (GND) density) simultaneously, to predict microstructural character distributions during concurrent static annealing and superplastic deformation.

One of the main driving forces for dynamic recovery (DRV), recrystallization and phase transformation is the stored dislocation density. However, due to the limitations in the

currently available dislocation density characterization tools, such as the small sampling areas by transmission electron microscope (TEM) [17,18] which can lead to poor statistical representation of the bulk [19], limited facility access for x-ray synchrotron [20], bulk measurement by x-ray diffraction [21], and etc., virtually no direct observation of dislocation density effects on various dynamic processes during superplastic forming has been obtained. Historically, sample (thin foil) preparation for TEM analysis has been performed using electropolishing or ion milling. TEM thin foil analysis of dislocations still has a number of significant limitations that are inherent to the thin foil approach *e.g.*, ion milling can lead to the point defects which in turn alters the state of the dislocations, similarly bulk thinning prior to electropolishing may generate dislocations through deformation [22]. Consequently, most TEM analysis of dislocation structures in deformed materials are performed after deformation, which makes it impossible to accurately correlate pre- and post-deformation morphologies in the context of specific microstructural characteristics [22].

The recent development of GND density estimation using EBSD, by measuring the lattice rotation and misorientation [23,24], makes the technique more promising for this purpose. It acquires a statistically representative data, high fidelity microstructure and GND density data to enable quantitative and qualitative analyzes. These will provide more insights into various dynamic processes during superplastic forming. Notes that EBSD can only estimates the GND density rather than the total dislocation density, as the statistically stored dislocation (SSD) density are not detectable by the technique. However, under typical superplastic forming conditions, in which the temperature is high and strain rate is low, the dislocation climb and cross-slip activities are considerably easier and profound compared to the cold forming condition. It is not unreasonable to assume that those dislocation climb and cross-slip would annihilate considerable number of SSDs, whereby the majority of the stored dislocations exist in the form of lower energy GNDs. Thus, the EBSD estimated GND density should be sufficient to represent the total dislocation density stored in the material during superplastic forming.

In this context, the aim of this study is to clarify how dynamic loading affects the microstructure evolution under superplastic forming conditions in a near- α titanium alloy by comparing the microstructure and GND density under static annealing and dynamic superplastic forming conditions. A better knowledge of the relative roles of each of these different conditions will improve the understanding of the superplasticity phenomena.

The route chosen was to trace and examine the gauge and grip regions of dog-bone shaped isothermal tensile test specimens under superplastic conditions. During superplastic deformation, the grip area was held by the crosshead, which experiences little to no deformation [8,25,26], whilst the specimen gauge area is exposed to significant strain. The grip and gauge regions were, however, exposed to the same temperature profile for the entire test duration [27]. Therefore, the grip region exhibits a microstructure associated with static annealing, whereas the gauge section exhibits a microstructure associated with dynamic superplastic loading [13]. The dynamic loading effects on dislocation density, dynamic

recrystallization, dynamic phase transformation, and grain rotation leading to textural changes were analyzed, and quantified. These results provide vital dataset for the development of physically based viscoplastic models of SPF in titanium alloys.

2. Materials and methods

2.1. Tensile testing

The material used in these investigations was TA15 (Ti–6Al–2Zr–1Mo–1V), which is a near- α titanium alloy, supplied in the form of sheets with 2 mm thickness. TA15 has wide applications in the aerospace industry because of its high strength to mass ratio, good weldability, and superior creep resistance at high temperature up to 550 °C, compared to other titanium alloys [28]. The β -transus temperature of TA15 alloy is 985 °C, which are determined by the chemical compositions of the alloy, provided in Table 1. Tensile specimens with a gauge length of 15 mm, the width of 6 mm, and thickness of 2 mm were cut parallel to the rolling direction (see Fig. 1b). The superplastic tensile tests were performed using aiLETRY-5kN electro-hydraulic servo mechanical testing machine (Fig. 1a). A conventional three-zone furnace was used to maintain a uniform target temperature throughout the tests. The temperature was monitored with thermocouples spot-welded to different positions on the tested specimen, as well as inside the upper and lower grip boxes. Additionally, the temperature was recorded and used by feedback control to ensure that the testing temperature kept within ± 3 °C of the target temperature. This enabled a higher accuracy in conducting the tests well within the ASTM standard for superplastic testing which allows a tolerance of ± 6 °C. The details of the testing protocol is provided in our previous work [28].

A schematic plot summarizing the detailed procedures for the superplastic tensile testing and heat treatment is presented in Fig. 1c. The heating rate is determined based on the average heating rate of a conventional furnace heating, whilst avoiding any possible temperature overshooting issues. The specimens were firstly heated at 5 °C/min up to a temperature 100 °C lower than the target temperature. A slow heating rate, 13 °C/min, was then applied until the specimens reached the target deformation temperature, T . The specimens were held at T for 15 minutes to eliminate any thermal gradient along the sample and to stabilize the furnace temperature distribution. Finally, the specimens were superplastically deformed at the designed temperatures and strain rates to various strain levels, followed by water quenching to freeze their microstructures.

Table 1 – Chemical compositions of TA15 alloy.

Element	Al	Zr	Mo	V	Ti
Mass%	6.78i	2.00	1.24	1.32	Bal.
Impurity	Fei	Si	C	Ni	
Mass%	0.050i	0.01i	0.0072i	0.0038i	

The deformation temperatures were 880 °C, 900 °C and 920 °C and strain rates were $0.01s^{-1}$, $0.001s^{-1}$ and $0.005s^{-1}$. The full matrix of the testing conditions (i.e., deformation temperatures, strain rates and strain levels) are given in detail in Table 2. Initially, a full continues test was conducted for each condition to final fracture to obtain the total elongation and the viscoelastic stress-strain curve. Then interrupted tests were carried out for each condition at selected strain levels, as given in Table 2, to examine the evolution of microstructure at intermediate strain levels.

2.2. Microstructure examination

The microstructures of the as-received and deformed samples were characterized using EBSD to investigate the superplastic deformation mechanisms. For each deformation condition, the EBSD samples were taken from the gauge regions (i.e., mechanically deformed) and the corresponding grip regions (i.e., non-deformed), where the heat treatment history was identical. The EBSD analysis was performed with a step size of 0.4 μm and a scan area of $248.4 \times 186.9 \mu\text{m}$. The α grain size, orientation maps, pole figures (PFs), inverse pole figures (IPFs), and geometrically necessary dislocations (GND) density were calculated.

The GND calculation process was based on the method described by Pantleon [29], using six available curvature tensors (i.e., five dislocation density tensors, and a tensor describing the difference between the dislocation tensors mutually). GND density was calculated using MATLAB™ toolbox MTEX with self-developed routines. A total of 33 potential dislocations are likely to present in the α phase including 3 types of $\langle a \rangle$ edge on basal planes, 3 types of $\langle a \rangle$ edge on prismatic planes, 6 types of $\langle a \rangle$ edge on pyramidal planes, 3 types of $\langle a \rangle$ screw dislocations, 12 types of $\langle a+c \rangle$ edge dislocations on first-order pyramidal slip planes, and 6 types of $\langle a+c \rangle$ screw dislocations. Various dislocation types have different line energies and therefore contributions to the total energy of the dislocations in the material. The line energy of each kind of dislocation was used as a weight; the objective function was to find the minimal weighted sum of all dislocation densities. According to Frank's rule, $E_{el} = \alpha G b^2$, where α is a constant, G is the shear modulus, b is the magnitude of the Burgers vector, the energy of a $\langle a+c \rangle$ edge dislocation is higher than a $\langle a \rangle$ edge dislocation by a factor of 3.51. The energy of a $\langle a \rangle$ edge dislocation is larger than $\langle a \rangle$ screw dislocation by a factor of $1/(1-\nu)$, where ν is the Poisson's ratio [30].

3. Results

3.1. Microstructure of the as-received material

The initial microstructure of the as-received material consists of a two-phase structure of α (dark region) and β (bright region) with typical equiaxed grains, as shown in the SEM micrograph in Fig. 2a. The volume fractions of α - and β -phases were estimated to be 94% and 6%, respectively, with the β -phase randomly distributed in α -phase matrix. A histogram of the

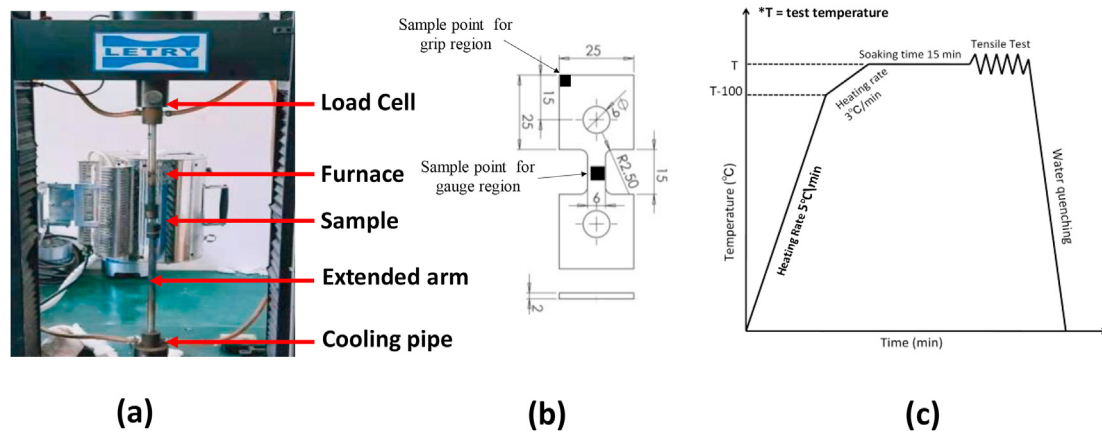


Fig. 1 – (a) Hot tensile testing system used in this study, (b) dimensions of uniaxial hot tensile specimen, and (c) schematic representation of thermo-mechanical processing route.

Table 2 – A summary of the interrupted tests carried out under various thermo-mechanical testing conditions for microstructure examinations.

Thermal Mechanical Testing Conditions (Temperature - °C & Strain Rate - s ⁻¹)	Stopping Stage (Stress - MPa & Strain)	Microstructural Analysis
880 °C & 0.01 s ⁻¹	A: 73.7 & 0.084 B: 64 & 1.05 C: 9 & 2.1	Microstructural Analysis is performed using EBSD technique to study the evolution of grain size, texture, grain boundaries & GND for the Stages A to L.
880 °C & 0.001 s ⁻¹	D: 53 & 0.174 E: 50 & 1.54 F: 18.5 & 2.27	
900 °C & 0.01 s ⁻¹	G: 22 & 0.18 H: 27 & 0.44 I: 50 & 2.67	
920 °C & 0.0005 s ⁻¹	J: 14 & 0.48 K: 15 & 0.74 L: 34.5 & 2.65	

grain size distribution shown in Fig. 2b displays the microstructure as predominantly equiaxed in morphology with an average grain size of 3.74 μm . Fig. 2c depicts an EBSD map with IPF coloring with respect to the normal direction (ND), showing the microstructure and texture distribution of the α phase in the as-received material. The EBSD IPF map of the initial microstructure shows fine equiaxed grains, with a preferred orientation, which is attributed to the rolling with insufficient subsequent annealing treatment. The plot of IPF in Fig. 2d reveals that the microstructure of the as-received sheet has strong textures, dominated by basal direction [0001] with maximum intensity of 4.9 (MRD), as also suggested by the presence of dominant red coloured grains within the microstructure in Fig. 2c. The presence of a strong preferred crystallographic texture of the α -phase in the as-received sheet is more clearly depicted by the basal {0001} pole figure presented in Fig. 2e. The {0001} pole figure indicates a strong transverse texture with the presence of basal component.

The GND distribution map of the same area is shown in Fig. 2f, where average GND is calculated as $3.47 \times 10^{14} \text{ m}^{-2}$ with a high standard deviation of $3.36 \times 10^{14} \text{ m}^{-2}$. This implies that the GND values for the as-received material have a widespread, ranging from grains with rare dislocations content to grains with high dislocation density. The EBSD pattern

quality map in Fig. 2g shows the fraction of low angle grain boundaries (LAGBs) (f_{LAGBs}) and high angle grain boundaries (HAGBs) (f_{HAGBs}) in the initial microstructure, with f_{HAGBs} and f_{LAGBs} estimated as 83% and 17%, respectively. In this study, HAGBs correspond to boundaries with misorientation angles higher than 15°, while LAGBs correspond to those with misorientation angle of 1–15°.

3.2. Tensile test results

The true-stress-strain curves for the hot tensile tests conducted at 880 °C/0.01s⁻¹, 900°C/0.01s⁻¹, 880i°C/0.001s⁻¹ and 920 °C/0.0005s⁻¹ are presented in Fig. 3. It is obvious from the flow curves that testing under higher strain rates at lower temperatures has led to an increased peak stress, while the opposite (i.e., lower strain rates at higher temperatures) has resulted in more elongation. For the former, the measured true stress response approaches a maximum stress (σ_{max}) just above the material's yield point. Once the σ_{max} is reached an immediate slope change is observed in the stress-strain curve where the material undergoes flow softening which is a function of the test temperature and strain rate. As previously found, dynamic recrystallization and the formation of voids result in apparent flow softening due to the nucleation and

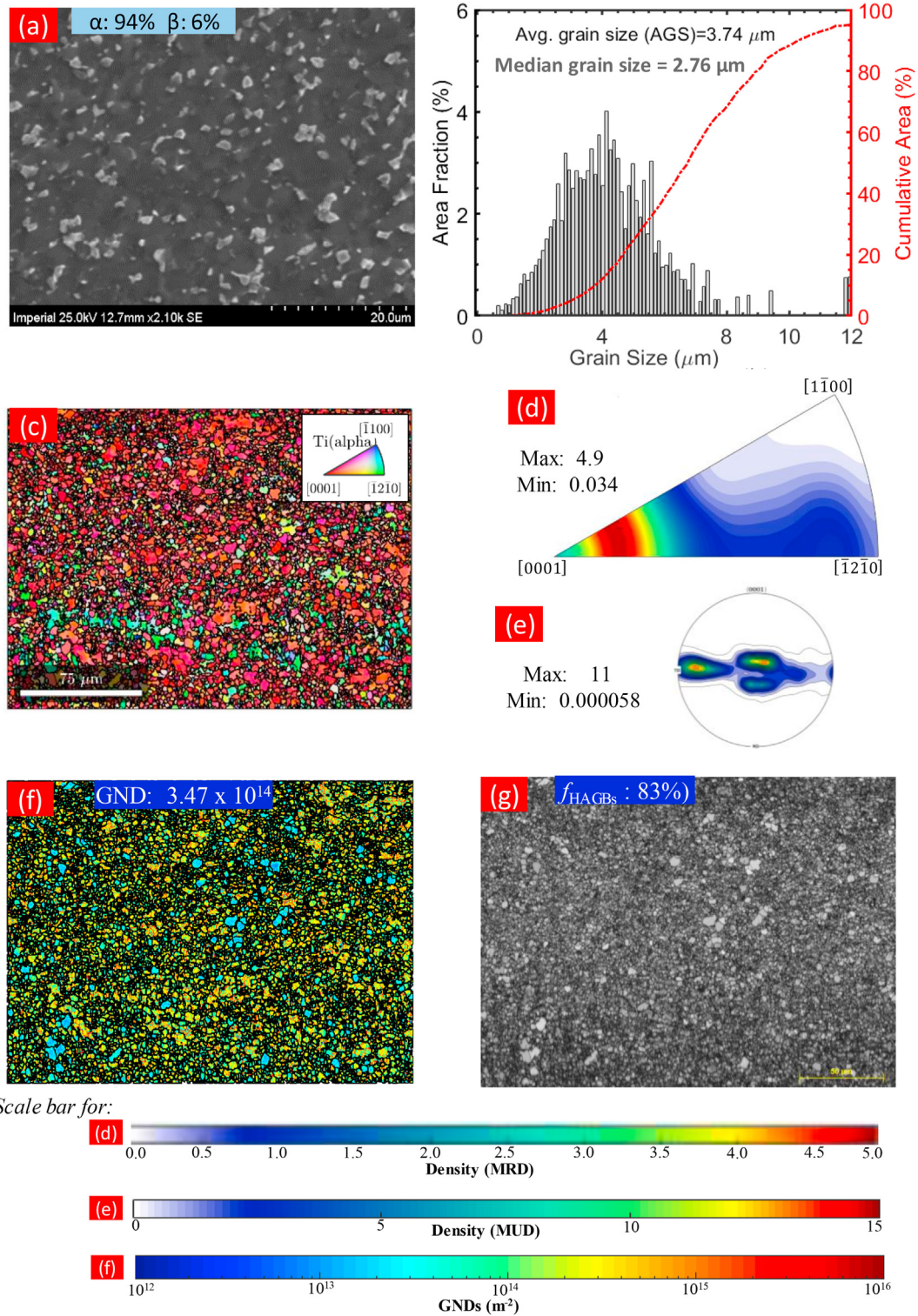


Fig. 2 – SEM and EBSD analyses of the microstructure of the as-received material:(a) SEM micrograph, (b) grain size distribution, (c) IPF coloured EBSD map w.r.t ND (d) corresponding IPF (e) {0001} (i.e., basal) pole figure showing the initial texture in α phase, (f) evaluated GND distribution map, and (g) pattern quality map of the same area as (c).

growth of new deformation free grains, and the coalescence of microscopic voids formed as a result of vacancy migration [31,32]. Hence, these measurements show that under higher strain rate (0.01s^{-1}) significant strain softening occurs, while applying lower strain rates of 0.001s^{-1} and 0.0005s^{-1} at higher

temperatures lead to strain hardening. Its apparent that there is a transition from a flow softening regime through an optimum steady-state plastic deformation region to a strain hardening regime by decreasing the strain rate from 0.001s^{-1} to 0.0005s^{-1} . Detailed microstructure analyses to further

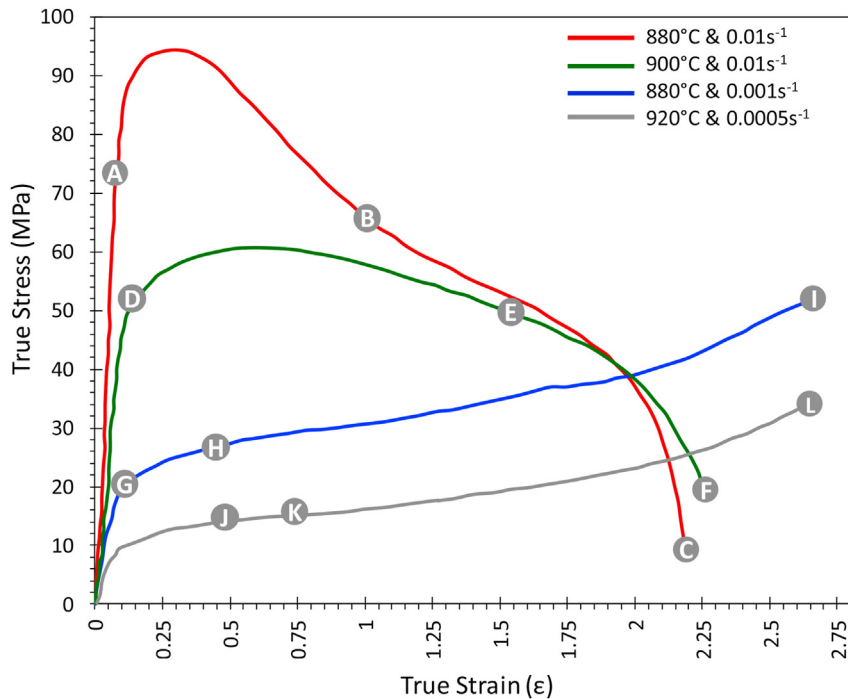


Fig. 3 – Measured true stress-true strain curves for the tested specimens at deformation temperature of 880 °C, 900 °C and 920 °C and under various strain rates.

confirm the underlying mechanisms are presented in the following sections.

3.3. Grain size evolution

Figure 4 shows plots of grain size distributions measured for the grip and gauge regions at different stages of thermo-mechanical tests under different conditions. For the tests interrupted at A to F, the morphology of grain size of in the gauge section deformed under 0.01s^{-1} strain rate changes from skewed to an almost normal distribution. However, in the grip regions of the same tests the distribution of grain sizes retained a degree of skewness from stages A to C. This changes to a normal distribution for stages D to F. For the deformation stages C, E, F, G, H, and J, the average grain size in the gauge regions are smaller than those in the grip regions. In contrast, for the rest of the deformation of stages, the grain sizes of the grip regions are smaller than those in the gauge regions. Under the higher strain rate of 0.01s^{-1} no significant grain growth takes places for all temperatures. In the gauge region, for deformation conditions of $880\text{ °C}/0.01\text{s}^{-1}$ it can be observed that moving from stage A to C, the average grain size decrease from $7.92\text{ }\mu\text{m}$ to $3.90\text{ }\mu\text{m}$. This agrees with the flow softening behavior in the corresponding stress-strain curve (see Fig. 3). On the other hand, in the grip region the grain sizes measured for stages A to C are almost similar, with a slight decrease (i.e., $5.56\text{ }\mu\text{m}$ – $5.23\text{ }\mu\text{m}$).

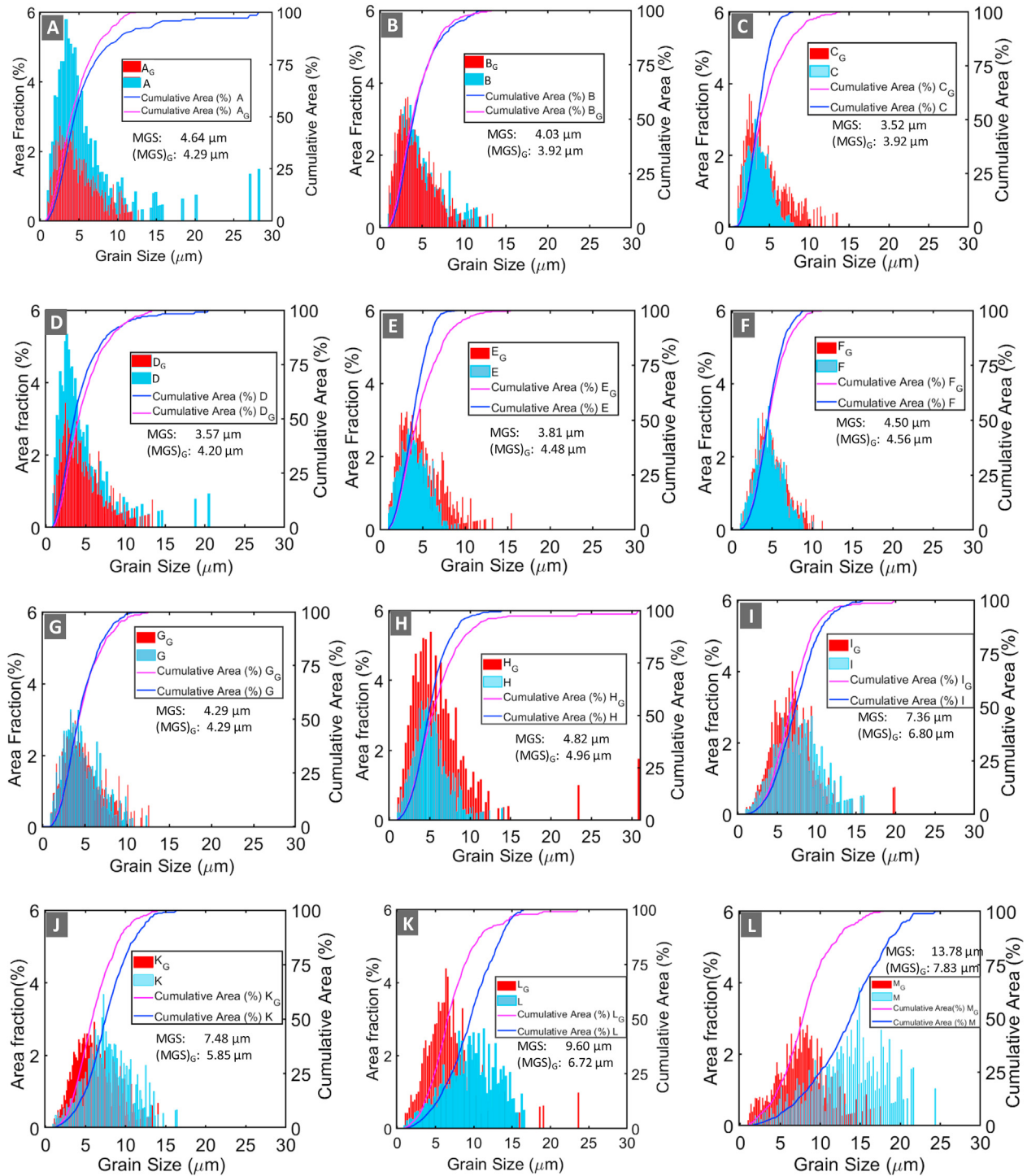
Comparison between the grain size evolution in the grip and the gauge regions showed that the final grain size in the gauge region increases with increasing deformation temperature and/or decreasing strain rate. In the grip region, however, under a constant strain rate of 0.01s^{-1} the grain size was slightly increased at both high (900 °C) and low

(880 °C) deformation temperatures. On the other hand, under the lower strain rates of 0.001s^{-1} and 0.0005s^{-1} , a considerable increase in the grain size is measured for all deformation temperatures in both grip and gauge regions, with that of the gauge region being more pronounced. The grains do, however, remain essentially equiaxed in both regions.

3.4. Texture evolution and recrystallization

In superplastic deformation, texture evolution is completely different from that under other non-superplastic forming conditions. This is because changes in the texture can be used to understand the likely deformation mechanisms active during the forming process. For example, grain boundary sliding (GBS) phenomenon is one of the SPF mechanisms during which the deformation is accommodated by both diffusion and slip. While the former might result in texture weakening due to random grain rotations [33], the latter may lead to changes in texture [34].

Figure 5 and Fig. 6 respectively show the IPF colored grain orientation maps with respect to ND, and their corresponding IPFs and $\{0001\}$ pole figures for the grip and the gauge regions under different deformation conditions. The color codes represent the crystal orientations of the α grains, red for $\{0\ 0\ 1\}$, green for $\{\bar{1}2\bar{1}0\}$ and blue for $\{\bar{1}100\}$, shown in the standard stereographic triangle. The texture intensities from the color bars are expressed in multiples of random distribution (MRD) and multiples of the uniform density (MUD) for the IPF and the pole figures, respectively. Under all testing conditions, the measured texture present in the grip region is quite different from those measured for the gauge region. The



*Subscript *G* denotes grip region *MGS denotes median grain size
 *The labels A, B, ...L denote the interrupted stages of the tensile tests

Fig. 4 – Evolution of grain size in TA15 during superplastic deformation measured after interrupted tests at stages A, B, ... L of the stress-strain curves highlighted in Fig. 3.

texture in the grip region changes only slightly from that of the as-received material (see Fig. 3d and e).

For the test conducted under 880 °C/0.01s⁻¹ condition, it is apparent that in the gauge region (see images A, B & C in Fig. 5) dynamic recrystallization (DRX) has initiated in stage A and its fraction increases with increasing the deformation level such

that when the final fracture occurs (i.e., stage C) the microstructure becomes fully recrystallized with random grain orientations. This is clear from the pole figures where strong weakening of the texture occurs from stages A through to C and results in a randomized texture. On the other hand, no apparent recrystallization can be observed for the grip region



Fig. 5 – EBSD IPF colouring with respect to ND showing microstructure evolution in TA15 during superplastic forming in the gauge and the grip regions. (The labels A, B, ...L denote the interrupted stages of the tensile tests highlighted in Fig. 3).

(i.e., A, B, & C in Fig. 6), where the final stage (i.e., stage C_D) still shows a heterogeneous microstructure.

Under the constant strain rate of 0.01s^{-1} an increase in the temperature from $880\text{ }^{\circ}\text{C}$ to $900\text{ }^{\circ}\text{C}$ has led to a significant increase in DRX in the gauge area, as shown in Fig. 5 for D, E & F for the gauge region. This is evident from the dominant presence of fine recrystallized equiaxed grains replacing the coarse deformed grains. At $900\text{ }^{\circ}\text{C}$, similarly to $880\text{ }^{\circ}\text{C}$, the

extent of static recrystallization (SRX) is also slightly higher in the grip region (see images D, E, & F in Fig. 5 for the grip regions). The occurrence of SRX in the grip regions at $900\text{ }^{\circ}\text{C}$, as evidenced by the randomized textures from D to F in Fig. 6, is attributed to the effect of thermal energy which leads to static annealing. It can be deduced that as the deformation continues from stage D to stage F, the maximum texture intensity of the gauge region decreases monotonously from 5.2 to 1.4

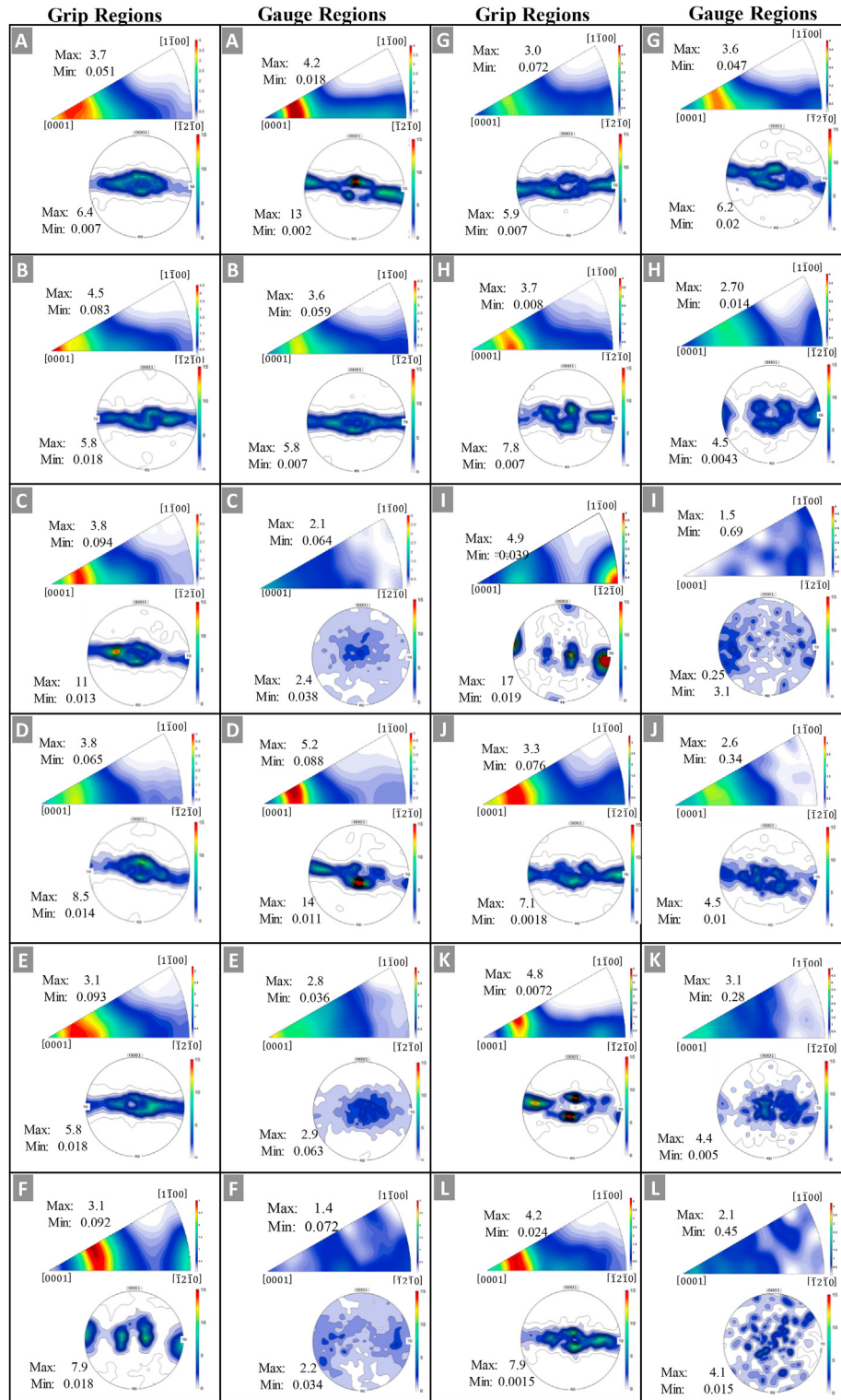


Fig. 6 – Texture evolution in TA15 during tensile testing under superplastic forming conditions at the grip and gauge regions. (The labels A, B, ...L denote the interrupted stages of the tensile tests highlighted in Fig. 3).

and leads to weakening and full randomization of the initial texture. The strong basal plane texture [0 0 0 1], in stage D has completely disappeared in stage F. At the same time, there is a little weakening of texture in the grip region throughout the tests (i.e., from stage D through E to F in Fig. 6).

For the test carried out under 920 °C/0.0005s⁻¹ condition (see Fig. 6), the texture randomization of the gauge region is achieved at a very early stage of deformation, i.e., the maximum texture intensity at stage J drops to 2.6 which indicates randomization of the initial texture. From stage J

onward until the final fracture at stage L, no significant changes in texture intensity is measured (see Fig. 6). This can be attributed to the dynamic grain growth which hinders GBS phenomenon and hence grain rotation. The grain orientation map of the gauge regions shown in images G, H, & I in Fig. 6, also supports this argument as no drastic changes in texture has occurred beyond stage J. It can be observed that recrystallization in the gauge region has been completed by stage J, whereby grain growth becomes more dominant thereafter rather than further recrystallization. The maximized level of DRX under the lowest strain rate and the highest temperature condition is mainly attributed to the longer exposure of the microstructure to higher deformation temperature, which is 4278 s at 0.48 strain. The same exposure time to a high temperature also causes significant recrystallization in the grip regions (see images J, K, & L in Fig. 5 for the grip regions). However, the grains are more heterogeneous in the grip area compared to those in the gauge region of the same condition.

It is interesting to note that the higher the strain level, the less elongated the grains become. Also, under all testing conditions, the grain orientation maps of the gauge region show a slight elongation in the grains along the tensile direction at initial and intermediate stages of deformation. Though, the grains in the gauge region have eventually become fully equiaxed by the end of the test (i.e., at fracture stage). Meanwhile, it is also evident that the grains in the gauge regions oriented in the {0001} direction (i.e., red grains in the orientation maps) gradually randomized with an increase in the strain level. Once a threshold strain is reached, the grains with $\{1100\}$ and even {0001} orientations tend to rotate in the $\{\bar{1}210\}$ crystallographic directions [35]. As a result, the preferential texture in the gauge region becomes weakened or completely randomized, while this is not the case for the grip regions.

3.5. GND evolution

Comparative quantitative illustrations of GND evolution in the grip and gauge regions under different thermo-mechanical conditions are shown in Fig. 7. For all testing conditions, the evaluated GND densities for the gauge region are smaller than those of the grip region, except for stages A and D where the dislocation density of the gauge region is higher than that of the corresponding grip region by 200% and 135%, respectively. For both A and D conditions, there is a drastic increase in the flow stress at the beginning of deformation (see Fig. 3) which is an evidence of the interaction and multiplication of dislocations.

Generally, these results suggest that for both the grip and the gauge regions, the decrease in dislocation density is greatly affected by strain rate (hence annealing time), while the variation in the deformation temperature has only a trivial effect on the evolution of GND. As shown in Fig. 7, the GND of the gauge region in stage A indicates large grains with small dislocation densities, as signified by the blue color. Also, there are small grains appear to be dislocation free, which is an evidence of the creation of new recrystallized grains.

In addition to the GND, the percentage of HAGBs is also used to study the difference between the regions under static annealing and superplastic deformation conditions. Fig. 8

shows EBSD pattern quality maps illustrating the evolution of HAGBs in the grip and gauge regions at different stages. The HAGBs and LAGBs were defined as boundaries with misorientation angles higher than 15° , and between 1 and 15° , respectively. The fraction of HAGBs in both the grip and the gauge regions have increased, compared to 83% in the as-received material (Fig. 2g). Under all testing conditions, the evolution of the fraction of HAGBs in the gauge region is drastically different from that of the corresponding grip region (Fig. 8). This implies that the microstructure evolution mechanisms are different in both regions. In the gauge region, the fraction of HAGBs increases monotonously with strain, while in the grip region the fraction of HAGBs decreases with increasing strain, except for the test carried out under $920^\circ\text{C}/0.0005\text{ s}^{-1}$ which had an almost steady behavior (see Fig. 8).

Comparison between the fractions of HAGBs measured for stages A & B to those of stages D & E (i.e., samples deformed at the same temperatures but different strain rates), shows that the fraction of LAGBs is relatively high for the tests underwent the lower strain rates. This is mainly because the sub-grain boundaries have insufficient time under higher strain rates to absorb enough dislocations for transformation to HAGBs.

4. Discussion

4.1. Microstructural evolution mechanisms

Based on the material's thermo-mechanical response (Fig. 3) and the microstructural observations (Figs. 4–8), the likely mechanisms for microstructure evolution under both thermal (i.e., the grip region) and thermal-mechanical (i.e., the gauge region) conditions during superplastic deformation of TA15 alloy can be classified as functions of temperature and strain rate as illustrated schematically in Fig. 9. Further details on the progress of microstructural evolution at different stages of each testing conditions, i.e., taking into consideration the effect of test duration, are illustrated in Fig. 10 (a & b). These observations cover the strain rate range of $0.0005\text{--}0.01\text{ s}^{-1}$ over a temperature range of $880\text{--}920^\circ\text{C}$.

At early stages of deformation at 880°C and 900°C under a relatively high strain rate of 0.01 s^{-1} (points A and D in Fig. 3), the majority of the plastic deformation is dominated by slip. This is manifested in the rolling texture intensity where almost no difference is measured between A and D in the grip region (i.e., 3.7 and 3.8 respectively) but that of the gauge region is significantly increased from 4.2 to 5.2. There is also a corresponding increase in the GND of the gauge region compared to that of the grip region. This implies that only dynamic recovery (DRV) was active in the grip region, in which the initially stored dislocations were cancelled out via climb and cross-slip operations.

At later stages of deformation (i.e., from B to C and E to F), there is a relative drop in the measured texture intensity for the gauge region compared to that of the grip region suggesting the initiation of GBS/grain rotation at later stages of the tests under relatively high strain rate [34]. This is also supported by the decrease in the evaluated values for the GND of the gauge region compared to the corresponding values for

the grip region. This is because superplastic deformation is generally associated with a decrease in dislocation activity [28]. For instance the initial rolling texture of the undeformed material in the grip region, from point A to point C is maintained.

Under the testing condition at $880\text{ }^{\circ}\text{C}/0.01\text{s}^{-1}$, the initial stages of the SRX/SRV and grain nucleation are initiated in the

grip region from A to C, however, more strain energy and annealing time were required to complete the next stage of the grain refinement. On the other hand, in the gauge region, the grains were fully refined by reaching the C stage. This implies that dynamic loading increases the recrystallization kinetic, which can be observed in the similarities between the microstructure of the grip region at stage C and that of the

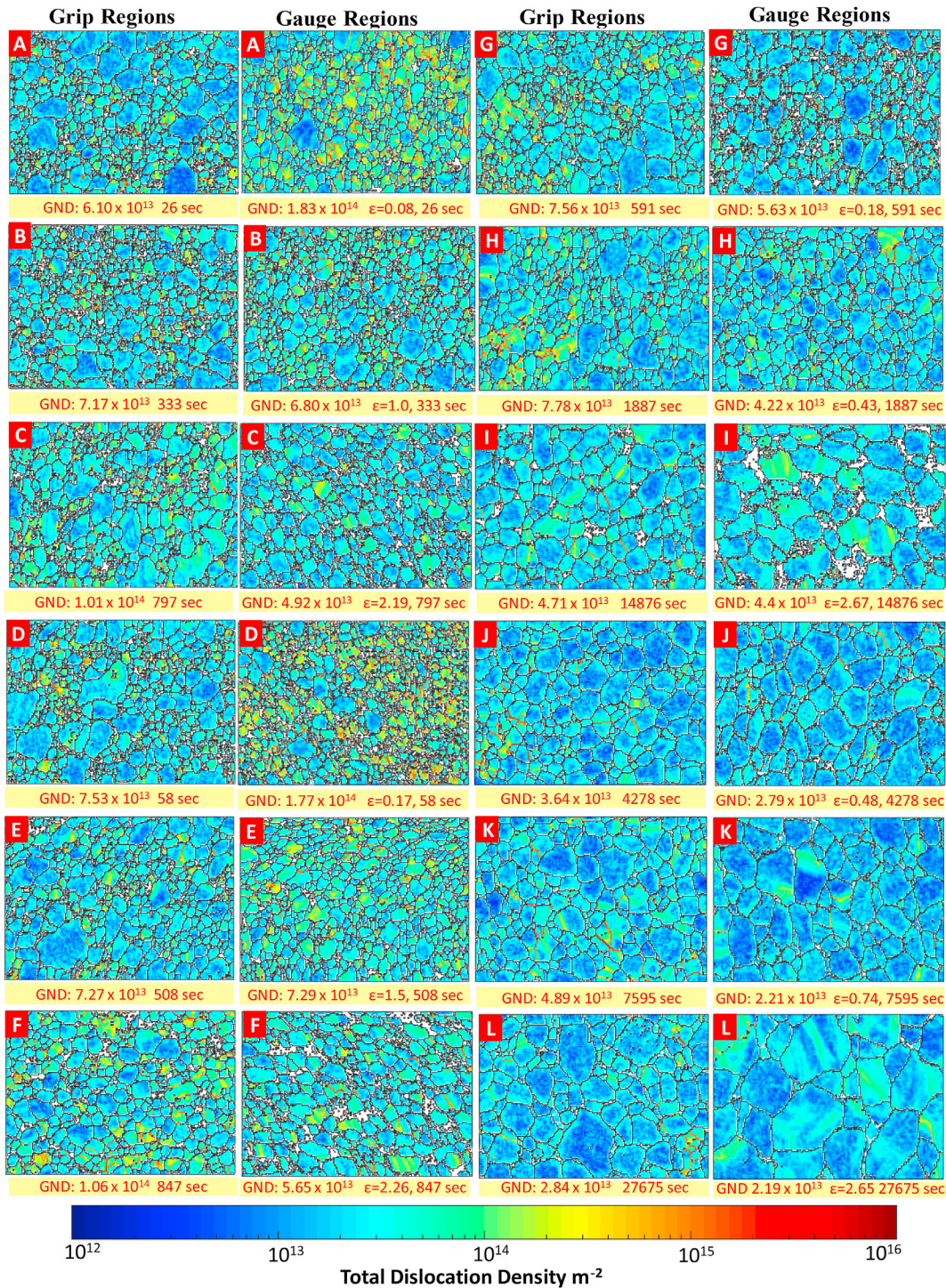


Fig. 7 – The evolution of GND in TA15 during testing under SPF conditions at the grips (i.e., static annealing) and the gauge (i.e., dynamic deformation) regions of the samples. The labels A, B, through to L denote the interrupted stages of the tensile tests from which EBSD maps were acquired (see Fig. 3).

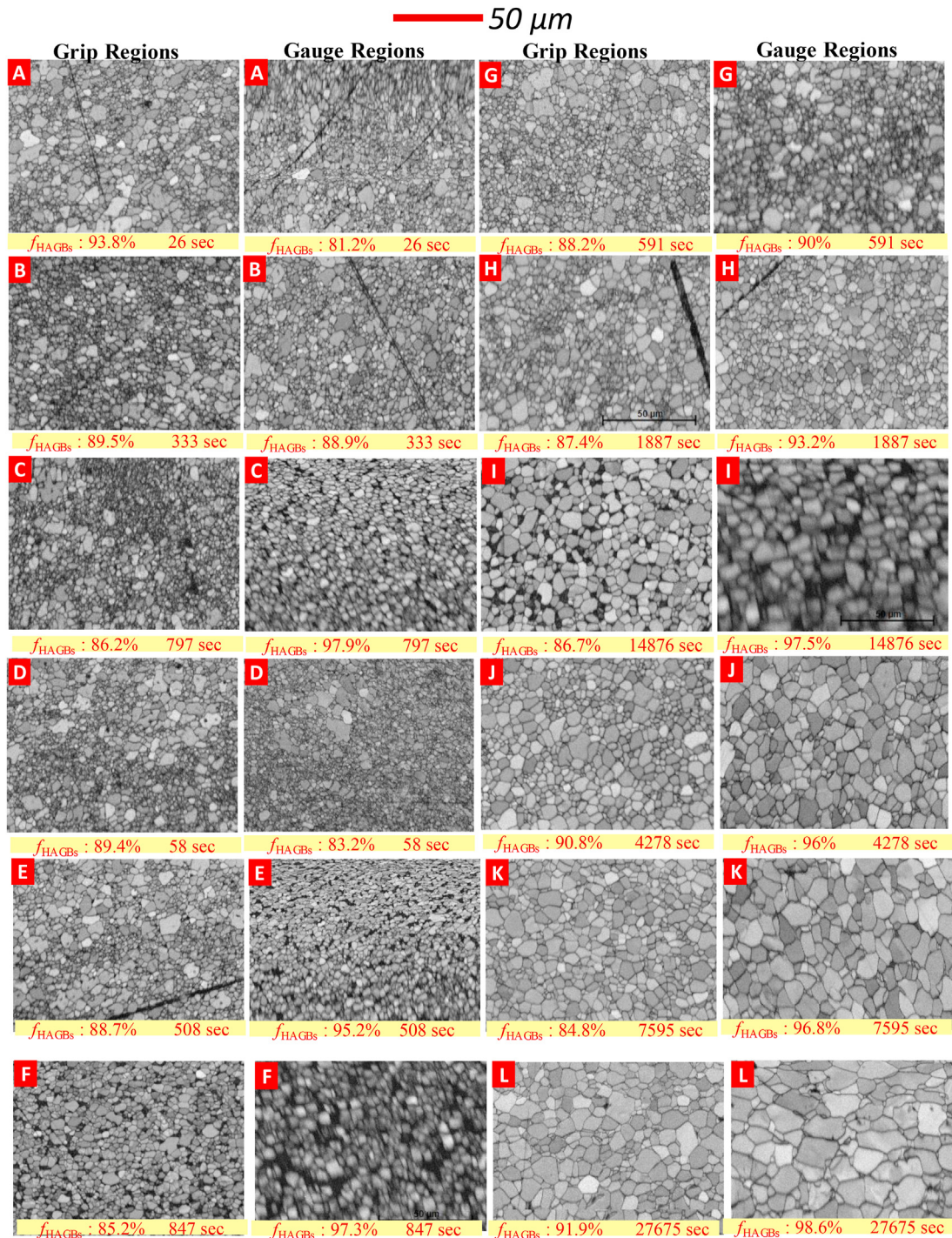


Fig. 8 – EBSD pattern quality maps showing the evolution of HAGBs in TA15 under SPF testing conditions at both the grip and gauge regions of the samples. The labels A, B, through to L denote the interrupted stages of the tensile tests (see Fig. 3) from which the results are obtained.

gauge region at stage B in Fig. 3. The refined microstructure was achieved in the gauge region after a dynamic annealing time of 333 s, whereas for the grip region after a static annealing time of 797 s, i.e., over twice as long.

The above explanations also stands for the testing condition of 900 °C/0.01s⁻¹, where a slight additional grain growth occurred with an increase in the test temperature.

Considering the grip region at the deformation temperature of 880 °C, decreasing the strain rate from 0.01s⁻¹ to 0.001s⁻¹ has provided the material with more annealing time. Hence, under this relatively slower strain rate (0.001s⁻¹) all the stages of static recrystallization, including recovery, refinement, and grain growth, appear to be completed. Note that with the decrease in the strain rate, the initial rolling texture

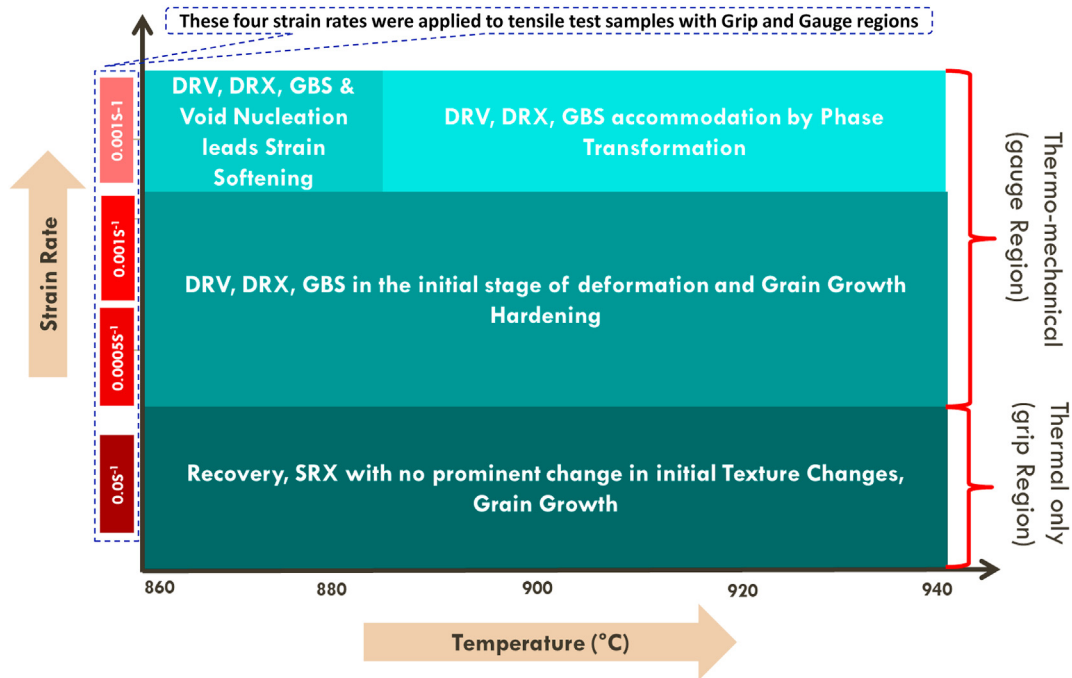


Fig. 9 – A deformation plot for the TA15 alloy classifying different deformation regimes based on temperature and strain rate.

of the material is maintained in the grip region even after exposure to a longer annealing time (i.e., 14,876 s for I). However, in the gauge region the texture has become entirely randomized, supporting the activation of GBS and grain rotation [34]. Comparison between the microstructures of the grip and the gauge regions under 0.001s^{-1} strain rate at stage G show that the microstructural evolutionary mechanisms of recovery and nucleation of new grains have initiated at the very beginning of the test. As a result, grain growth has also been observed at these early stages of tensile testing. Here the growth in small grains is observed at the expense of the large grains. At the same time, some of the large grains were merged with smaller grains, leading to an equiaxed and homogenous microstructure.

No significant difference was observed between the microstructure and grain size of the gauge region with those of the grip region under the deformation condition of $880\text{ °C}/0.001\text{s}^{-1}$. This may be due to the small flow stress under the lower strain rate of 0.001s^{-1} , thus resulting in a decrease in the grain boundary migration rate and also lower level of dynamic recrystallization. The flow stress may only drive the grain boundary rotation and sliding rather than boundary migration, as the energy difference in terms of dislocation density across the boundaries would be very small at lower flow stress levels [36]. This is also supported by the microstructural observations made for the grip and the corresponding gauge regions for the testing condition $880\text{ °C}/0.01\text{s}^{-1}$, where the rate of dynamic recrystallization at the gauge region was faster than that of the grip region, possibly because of the higher flow stresses attained under higher strain rates. It can be deduced from these observations that the higher flow stresses enhance the rate of grain boundary migration and hence recrystallization.

Under the testing condition of $920\text{ °C}/0.0005\text{s}^{-1}$, the high thermal energy delivered to the material at higher

temperature leads to the completion of the recrystallization process during the 15 min soak time in the beginning of the test, which appears to be SRX in nature. Therefore, during the rest of the test stages, only grain growth was observed for both the grip and the gauge regions. Similarly to the grip regions of all other tests, the initial undeformed rolling texture was retained for the grip region of this test as well. For the gauge region, however, the texture intensity was decreased at the beginning of the test (stage J), with texture developing at the later stages (stages K and L) due to grain growth. The grain growth is further enhanced by the process of grain rotation. Because of the importance of GBS and grain rotation for superplasticity, there is a possibility of grain “coalescence” to occur during deformation [37]. This occurs when the neighboring grains rotate such that the misorientation between them is eliminated, which then leads to the elimination of the boundary between them. Following the coalescence, some local migration of the surrounding boundaries is likely to occur [38]. This mechanism can produce an increase in grain size with strain and an increase in texture intensity, differing from the texture of the original rolled plate [39]. Fig. 11 summarizes the evolution of various microstructure characteristics quantitatively in both the grip and the gauge regions of TA15 samples.

4.2. Grain size evolution

The evolution of grain size has occurred over several recrystallization phases including, Phase (i) dislocation annihilation by DRV, Phase (ii) nucleation of new grains, Phase (iii) grains refinement through absorption of small grains by larger grains, or the appearance of cell structures within large grains, and Phase (iv) normal grain growth to further reduce the grain boundary energy.

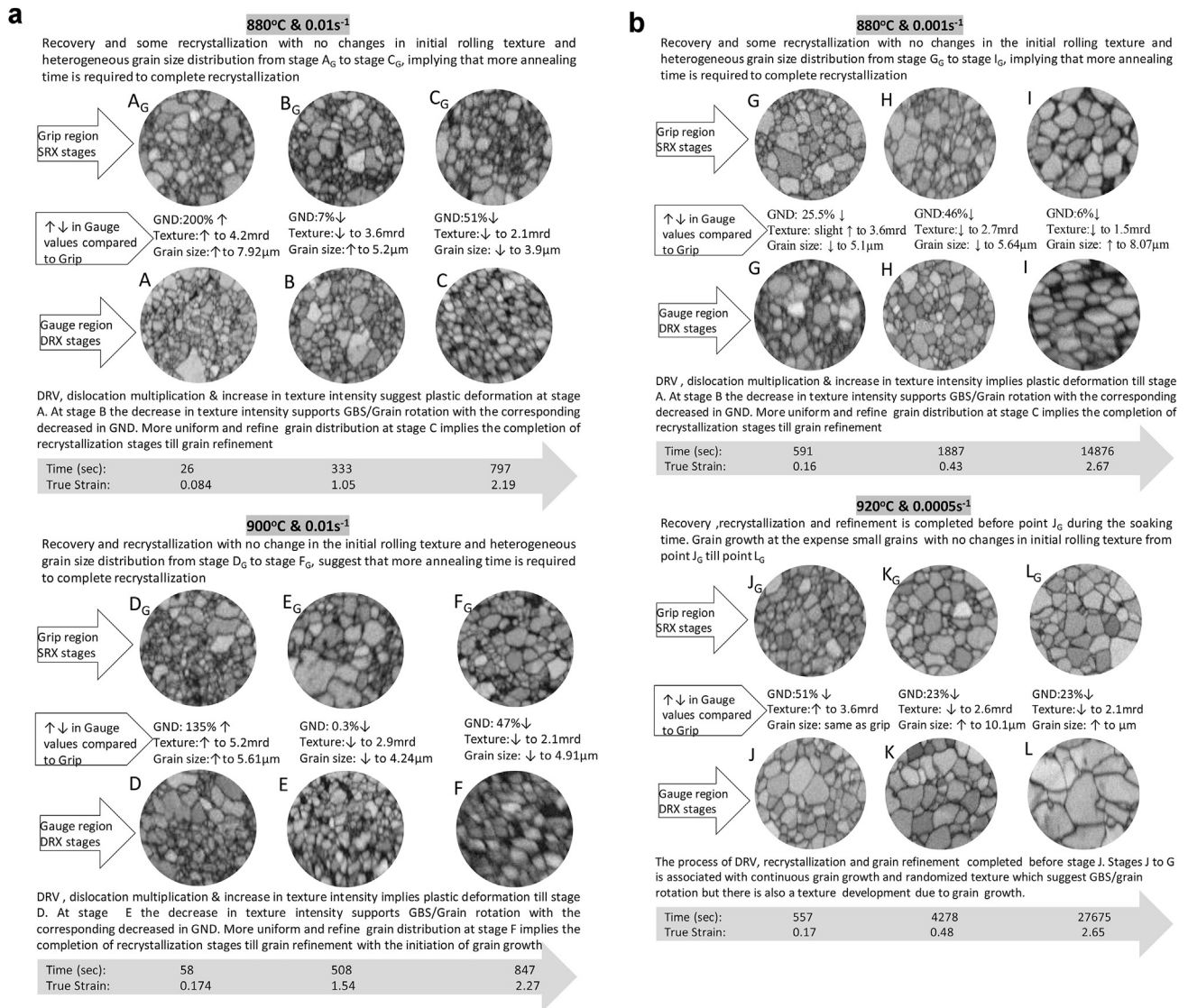


Fig. 10 – a. The likely mechanisms of microstructural evolution under static annealing (the grip region) and dynamic annealing (the gauge region) process during superplastic deformation of TA15 alloy at temperatures 880 °C – 900 °C under a strain rate of 0.01s⁻¹. b. The likely mechanism of microstructural evolution under static annealing (the grip region) and dynamic annealing (the gauge region) during superplastic deformation of TA15 alloy at temperatures 880 °C and 920 °C under strain rates of 0.001s⁻¹ and 0.0005s⁻¹, respectively.

Figure 11b shows that the final recrystallization phase of grain growth is activated for both the grip and the gauge regions (i.e., static and dynamic conditions) under strain rates of 0.001s⁻¹ and 0.0005s⁻¹. On the other hand, for the tests conducted under 0.01s⁻¹, grain refinement (Phase-i) was achieved for the gauge region whereas in the grip region Phases i, ii & iii were still carrying on simultaneously.

It was observed that at the deformation stages C, E, F, G, H, and J, the average grain size in gauge region was smaller than that of the grip region. In contrast, at the rest of the deformation of stages, the grain size measured for the grip region was smaller than that for the gauge regions. A possible interpretation for the larger grain size of the grip region compared to that of the gauge region under given deformation conditions can be related to DRX during superplastic deformation. As shown in Fig. 3, under the higher strain rate (0.01s⁻¹), the material in the

gauge region shows an apparent strain-softening behavior beyond true strains >0.33 and > 0.74 at 880 °C and 900 °C, respectively. This can be partially due to DRX and also the formation and coalescence of voids during the superplastic deformation. The low ductility and strain-softening measured for these tests under the 0.01 s⁻¹ strain rate has previously been shown for Ti-6Al-4V to be due to the formation of cavitation and their growth beyond a threshold value that leads to a premature failure [5,31]. Post-mortem study of voids formed under similar conditions confirmed that the size and volume fraction of the cavities under higher strain rates were found to be significantly larger than those of the tests that exhibited steady state superplastic forming [31]. On the other hand, microstructures in the grip region are only governed by grain growth [40] since DRX cannot take place under static conditions. Therefore, microstructures in the grip region was coarser

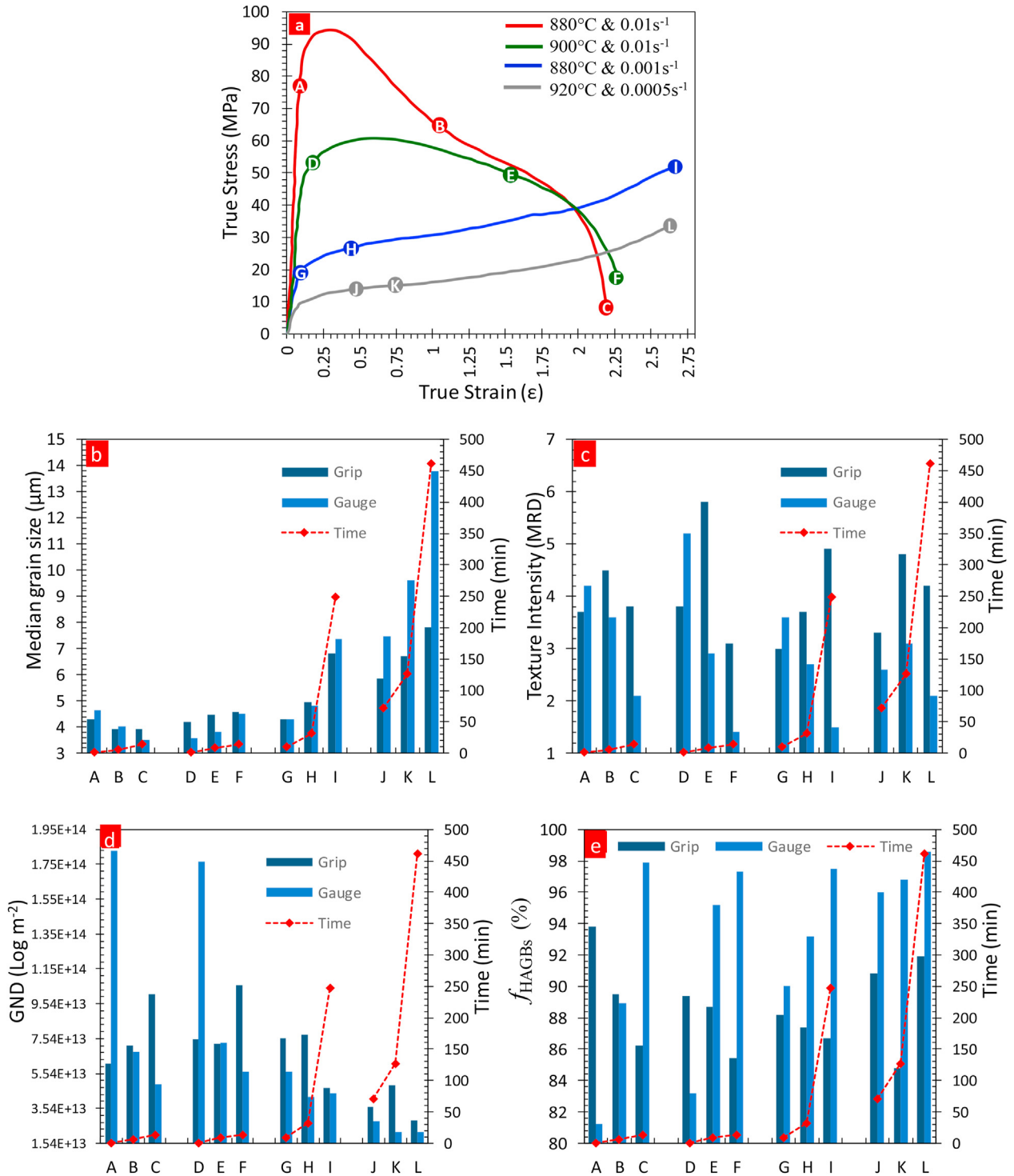


Fig. 11 – Quantitative analyses of the evolutions of microstructure characteristics during testing under SPF conditions in both the grip and gauge regions, (a) True stress-strain curves (b) grain size (c) crystallographic texture, (d) GND, and (e) HAGBs.

than those in the gauge region. Due to the competition between DRX and the concurrent grain growth process, the grain size in the gauge region did not change significantly.

For the tests subjected to relatively low strain rates, both the grip and the gauge regions were exposed to high temperature for an extended period comparatively, and hence the

grains had enough time to grow through thermally initiated mechanisms. It can be seen from Fig. 5 that at the deformation stages G, H, ..., L (i.e., associated with different stages of the tests conducted under low strain rates $0.001s^{-1}$ and $0.0005s^{-1}$), grain growth in both regions was initiated at the beginning of the superplastic deformation, resulting in an increase in grain

size with increasing strain. The superplastic deformation mechanism is believed to be controlled by a competition between DRX and dynamic grain growth [41]. The strain hardening characteristic under SPF conditions typically emerges from the higher impact of dynamic grain growth compared to that of grain refinement due to DRX [5,31]. The presence of coarser final grain size in the gauge region compared to that of the grip region indicates that dynamic grain growth was more prevalent than grain refinement by DRX under a given SPF condition [42]. These observations (i.e., coarser final grain size in the gauge region compared to that of the grip region) contradicts the results of previous studies on other alloys [12,13,15,16]. The possible reason for this contradiction can be due to a slight difference in the applied SPF conditions (e.g., slightly higher strain rate) which can lead to the dominance of GBS compared to grain growth, and as a result leading to a steady state deformation with negligible level of strain hardening in the stress-stress curves in those previous studies. The effect of changes in strain rate and temperature on deformation mechanisms and consequently on SPF behaviors are shown schematically in Fig. 9.

At stages B and C, a continuous decrease in grains number is evident (see Fig. 9) for the grip region, indicating that Phase i and ii of recrystallization were operational. This is supported by the plots of GND distribution in Fig. 7 which shows that the distribution of GND in the grip region was not uniform, similarly to the as-received material in which small grains contain more dislocations compared to larger grains. For the corresponding gauge region at B, the number of grains was reduced further, and the GND distribution became very similar to that of the gauge region at stage A (see Fig. 11). Similar explanations stands for the grip regions at stages D, E and F.

In the gauge region at stages D, E, F, however, the grain refinement phase (Phase-iii) was completed in-between E and F. The drop in the grain size measured at F (see Fig. 9) can be attributed to the initiation of Phase-iv, i.e., grain growth, which indicated the termination of grain refinement mechanisms (Phase-iii).

At early stages (i.e., G and H) of the tests carried out under $880\text{ }^{\circ}\text{C}/0.001\text{s}^{-1}$, the grain size has increased in the grip region (see Fig. 9). The distribution of the grain size in the grip and the gauge regions at G look similarly to those of the grip region at C and D. This is due to the longer exposure time of the grip and the gauge regions at G, where Phases-i, ii & iii of recrystallization were completed and grain growth (i.e., Phase-iv) progressed as the test continued to stages H and I. The grain growth rate must have been higher in the gauge region compared to the grip region due to the additional strain energy input on top of thermal energy. At stages J, K, and L, the grain size in the grip region (e.g., 2849 at J) was smaller than that of the as-received material by two folds. This was because at these stages both the grip and the gauge regions underwent Phase-iv of recrystallization due to high thermal energy (i.e., high temperature $920\text{ }^{\circ}\text{C}$) input and longer aging time (i.e., low strain rate 0.0005s^{-1}).

In summary, for the specimens tested under the lower strain rates of 0.001s^{-1} and 0.0005s^{-1} , the data obtained from the grip regions revealed the occurrence of limited time-induced grain growth. On the other hand, the microstructure of the corresponding gauge regions exhibited deformation-induced grain growth under these conditions. As expected,

under these relatively lower strain rates, the grain coarsening rate in the gauge region was greater than that in the grip region. This is usually associated with GBS and an increase in the grain boundary migration rate by the imposed stress under SPF conditions. This implies that the applied stress imposed on the HAGBs accelerate boundary migration rate rather than generating more dislocations. This is very different from the conventional thermal mechanical loading, where the applied stress mainly drives the dislocation activities to accommodate plastic strain. In the grip region the grain growth is generally thermally driven by the static annealing process where smaller grains are absorbed by the larger growing grains.

4.3. Texture evolution

From Fig. 11c, it can be seen that the texture intensity in the gauge region follows a decreasing trend with increasing strain, while that of the grip region remains similar to the texture of the as-received material. The initial texture in the gauge region is almost randomized, indicates that grain rotation has occurred, leading to the weakening of texture.

The observed changes in texture intensity of the gauge region are closely related to GBS phenomena [39], as random sliding events gives rise to a homogeneous decrease in texture [43]. This emphasis on possibility of using texture evolution to understand the likely deformation mechanism during SPF [34]. These results suggest that various mechanisms are active during SPF depending on the forming conditions (e.g., strain rate, temperature).

4.4. Evolution of GND & HAGBs

Form Fig. 10d, it can be observed that in the gauge region of all tests, the GND has a decreasing trend, which implies that the deformation was governed by GBS and grain rotation. The dislocation density can be controlled by the rate of dislocation absorption by grain boundaries [31]. As shown in Fig. 10d, a decrease in the strain rate enhanced the capacity of grain boundaries to absorb more dislocations, and this subsequently led to a relatively low level of GNDs in the gauge region compared to the grip region. The increase in the deformation temperature under a given strain rate increases the mobility of grain boundaries to absorb dislocations and results in a lower overall GND density in the material.

At lowest deformation temperature ($880\text{ }^{\circ}\text{C}$) and highest loading rate (0.01s^{-1}) channels like GND distributions can be found in the form of cellular or sub grain patterns/structures, which is evidence of continuous dynamic recrystallization (CDRX). CDRX has been reported before [37,40], as a dominated recovery process which proceeds by continuous absorption of lattice dislocations generated during the deformation process and grow into sub-grain boundaries without significant changes in the sub-grain size. This results in an increase in the misorientation angle between adjacent sub-grains [37,44]. These data suggest that for both the grip and gauge regions, the decrease in dislocation density is affected largely by strain rate (i.e., hence the annealing time), while the variation in the deformation temperature has a trivial impact on the evolution of GND.

For the higher strain rate of 0.01s^{-1} , the initial increase in GND in the gauge region at stages A and D can be explained by

work hardening, whereby dislocations were generated. These dislocations were subsequently absorbed by grain boundaries at later stages of plastic deformation due to the migration of HAGBs and the absorption of dislocations (see stages C & F in Fig. 7).

Under the lower strain rates of 0.001s^{-1} and 0.0005s^{-1} , the low stress levels leads to the generation of less number of dislocations in the grains, and therefore lower level of lower work hardening. This is due to the climb and cross-slip of the newly generated dislocations to cancel each other out as a result of long exposure time to high temperature. In the gauge regions of these tests at points H, I, K and L, the GND drops further, supporting the idea that GBS/grain rotation is the main deformation mechanism [43]. Under these strain rates, a higher GND density were measured in the grip regions, as seen at the fracture stages C and F (see Fig. 9), which can be due to the unavoidable material flow from the grip region into the gauge region during superplastic process [45].

The HAGBs are known as to have higher boundary energy than the LAGBs, which promotes the occurrence of the GBS mechanism during SPF [46,47]. HAGBs also ensure narrow distribution of equiaxed α grains due to globalization which in turn promotes softening behavior during hot tensile deformation [48,49]. The increase in HAGBs with increasing strain under lower strain rates of 0.001s^{-1} and 0.0005s^{-1} suggest that GBS can be the dominant deformation mechanism during SPF [7,50]. On the other hand, the increase in the fraction of HAGBs (i.e., from initial 83%–92%) in the grip region under $920\text{ }^{\circ}\text{C}/0.0005\text{s}^{-1}$ (Fig. 10e), where the material was exposed to high temperatures for a long duration of time with no strain, suggest that this phenomenon cannot only be the result of strain but also exposure to high temperature too. It is also evident from the grip samples exposed to deformation conditions of $880\text{ }^{\circ}\text{C}/0.01\text{s}^{-1}$, $900\text{ }^{\circ}\text{C}/0.01\text{s}^{-1}$ and $880\text{ }^{\circ}\text{C}/0.001\text{s}^{-1}$ that the conversion of LAGBs in the interior of fine equiaxed grains into more homogenous HAGBs is greatly affected by annealing at these temperatures.

5. Conclusion

The key conclusions can be drawn as:

- i. Superplastic deformation significantly reduced the initial rolling texture, demonstrating the characteristic grain rotation process. Under all testing conditions, the texture observed in the grip region was very different from that found in the gauge region. The maximum intensity of the texture observed in the grip region remained almost unchanged compared to that of the as-received material.
- ii. GND density values in the superplasticity deformed region (i.e., gauge) seemed to generally agree well with hardening and softening behavior shown in the measured stress-strain curves. At the early stages of deformation, GND density generally increase with lower temperatures and higher strain rates. After further deformation, GND density dropped, indicating the initiation of recrystallization.
- iii. The dynamic loading accelerated dynamic recrystallization and resulted in faster grain growth under lower

strain rates compared to static recrystallization. This led to considerably larger grain size in the gauge region compared to the grip regions.

- iv. The superplastic forming conditions led to differences in the evolution of the HAGBs fraction in the gauge region compared to the corresponding grip region, indicating that the microstructure evolution mechanisms were different. The fraction of HAGBs in both the grip and the gauge regions increased under all testing conditions.

Declaration of Competing Interest

The authors declare that they have no known competing financial interests or personal relationships that could have appeared to influence the work reported in this paper.

Acknowledgements

The authors acknowledge the financial support received from EPSRC LightForm program (EP/R001715/1) and UKAEA.

REFERENCES

- [1] Imai H, Yamane G, Matsumoto H, Vidal V, Velay V. Superplasticity of metastable ultrafine-grained Ti6242S alloy: mechanical flow behavior and microstructural evolution. *Mater Sci Eng, A* 2019;754:569–80.
- [2] Yasmeen T, Shao Z, Zhao L, Gao P, Lin J, Jiang J. Constitutive modeling for the simulation of the superplastic forming of TA15 titanium alloy. *Int J Mech Sci* 2019;164:105178.
- [3] Zhang W, Ding H, Cai M, Yang W, Li J. Ultra-grain refinement and enhanced low-temperature superplasticity in a friction stir-processed Ti-6Al-4V alloy. *Mater Sci Eng, A* 2018;727:90–6.
- [4] Tan MJ, Chen GW, Thiruvarduchelvan S. High temperature deformation in Ti-5Al-2.5 Sn alloy. *J Mater Process Technol* 2007;192:434–8.
- [5] Alabort E, Kontis P, Barba D, Dragnevski K, Reed RC. On the mechanisms of superplasticity in Ti-6Al-4V. *Acta Mater* 2016;105:449–63.
- [6] Zherebtsov SV, Kudryavtsev EA, Salishchev GA, Straumal BB, Semiatin SL. Microstructure evolution and mechanical behavior of ultrafine Ti6Al4V during low-temperature superplastic deformation. *Acta Mater* 2016;121:152–63.
- [7] Mikhaylovskaya AV, Mosleh AO, Kotov AD, Kwame JS, Pourcelet T, Golovin IS, et al. Superplastic deformation behaviour and microstructure evolution of near- α Ti-Al-Mn alloy. *Mater Sci Eng, A* 2017;708:469–77.
- [8] Motyka M, Sieniawski J, Ziaja W. Microstructural aspects of superplasticity in Ti-6Al-4V alloy. *Mater Sci Eng, A* 2014;599:57–63.
- [9] Yang KL, Huang JC, Wang YN. Phase transformation in the β phase of super $\alpha 2$ Ti3Al base alloys during static annealing and superplastic deformation at 700–1000° C. *Acta Mater* 2003;51(9):2577–94.
- [10] Friedman PA, Ghosh AK. Microstructural evolution and superplastic deformation behavior of fine grain 5083Al. *Metall Mater Trans* 1996;27(12):3827–39.
- [11] Kaibyshev R, Musin F, Lesuer DR, Nieh TG. Superplastic behavior of an Al-Mg alloy at elevated temperatures. *Mater Sci Eng, A* 2003;342(1–2):169–77.

- [12] Cao G, Zhang D, Chai F, Zhang W, Qiu C. Superplastic behavior and microstructure evolution of a fine-grained Mg–Y–Nd alloy processed by submerged friction stir processing. *Mater Sci Eng, A* 2015;642:157–66.
- [13] Chai F, Zhang D, Zhang W, Li Y. Microstructure evolution during high strain rate tensile deformation of a fine-grained AZ91 magnesium alloy. *Mater Sci Eng, A* 2014;590:80–7.
- [14] Kim WJ, Kim MJ, Wang JY. Superplastic behavior of a fine-grained ZK60 magnesium alloy processed by high-ratio differential speed rolling. *Mater Sci Eng, A* 2009;527(1–2):322–7.
- [15] Cepeda-Jiménez CM, García-Infanta JM, Ruano OA, Carreño F. Achieving microstructures prone to superplastic deformation in an Al–Zn–Mg–Cu alloy by equal channel angular pressing. *J Alloys Compd* 2013;546:253–9.
- [16] Vijayananth S, Jayaseelan V, Kumar NM. High temperature superplasticity and its deformation mechanism of AA6063/SiCp. *Case Stud Therm Eng* 2019;14:100479.
- [17] Brodusch N, Brahimi SV, Barbosa De Melo E, Song J, Yue S, Piché N, et al. Scanning Electron Microscopy versus Transmission Electron Microscopy for Material Characterization: A Comparative Study on High-Strength Steels. *Scanning*. 2021. 2021.
- [18] Pennycook SJ, David B, Williams CB. Transmission electron microscopy: a textbook for materials science. *Microsc Microanal* 2010;16(1):111.
- [19] Dunlap BE, Ruggles TJ, Fullwood DT, Jackson B, Crimp MA. Comparison of dislocation characterization by electron channeling contrast imaging and cross-correlation electron backscattered diffraction. *Ultramicroscopy* 2018;184:125–33.
- [20] Barabash RI, Ice G, editors. Strain and dislocation gradients from diffraction: spatially-resolved local structure and defects. World Scientific; 2014.
- [21] Tanner BK. Characterization of crystal growth defects by X-ray methods, 63. Springer Science & Business Media; 2013.
- [22] Crimp MA. Scanning electron microscopy imaging of dislocations in bulk materials, using electron channeling contrast. *Microsc Res Tech* 2006;69(5):374–81.
- [23] Jiang J, Britton TB, Wilkinson AJ. Measurement of geometrically necessary dislocation density with high resolution electron backscatter diffraction: effects of detector binning and step size. *Ultramicroscopy* 2013;125:1–9.
- [24] Jiang J, Britton TB, Wilkinson AJ. Evolution of dislocation density distributions in copper during tensile deformation. *Acta Mater* 2013;61(19):7227–39.
- [25] Du ZX, Liu JS, Jiang SD, Xiao SL, Kong FT, Chen YY. Strain rate dependence of microstructural evolution in β titanium alloy during subtransus superplastic deformation. *J Alloys Compd* 2015;647:1–5.
- [26] Fata A, Faraji G, Mashhadi MM, Tavakkoli V. Hot tensile deformation and fracture behavior of ultrafine-grained AZ31 magnesium alloy processed by severe plastic deformation. *Mater Sci Eng, A* 2016;674:9–17.
- [27] Mishra MK, Rao AG, Balasundar I, Kashyap BP, Prabhu N. On the microstructure evolution in friction stir processed 2507 super duplex stainless steel and its effect on tensile behaviour at ambient and elevated temperatures. *Mater Sci Eng, A* 2018;719:82–92.
- [28] Yasmeen T, Zhao B, Zheng JH, Tian F, Lin J, Jiang J. The study of flow behavior and governing mechanisms of a titanium alloy during superplastic forming. *Mater Sci Eng, A* 2020:139482.
- [29] Pantleon W. Resolving the geometrically necessary dislocation content by conventional electron backscattering diffraction. *Scripta Mater* 2008;58(11):994–7.
- [30] Hull D, Bacon DJ. Introduction to dislocations, 37. Elsevier; 2011.
- [31] da Silva L, Sivaswamy G, Sun L, Rahimi S. Effect of texture and mechanical anisotropy on flow behaviour in Ti–6Al–4V alloy under superplastic forming conditions. *Mater Sci Eng, A* 2021;819:141367.
- [32] Alabort E, Putman D, Reed RC. Superplasticity in Ti–6Al–4V: characterisation, modelling and applications. *Acta Mater* 2015;95:428–42.
- [33] Duan YL, Tang L, Deng Y, Cao XW, Xu GF, Yin ZM. Superplastic behavior and microstructure evolution of a new Al–Mg–Sc–Zr alloy subjected to a simple thermomechanical processing. *Mater Sci Eng, A* 2016;669:205–17.
- [34] Watanabe H, Kurimoto K, Uesugi T, Takigawa Y, Higashi K. Accommodation mechanisms for grain boundary sliding as inferred from texture evolution during superplastic deformation. *Phil Mag* 2013;93(22):2913–31.
- [35] Wang B, Deng L, Guo N, Xu Z, Li Q. EBSD analysis of {10–12} twinning activity in Mg–3Al–1Zn alloy during compression. *Mater Char* 2014;98:180–5.
- [36] Lin J, Liu Y. A set of unified constitutive equations for modelling microstructure evolution in hot deformation. *J Mater Process Technol* 2003;143:281–5.
- [37] Humphreys FJ, Rohrer GS, Rollett A. Recrystallization and related annealing phenomena. Elsevier; 2017.
- [38] Farkas D, Mohanty S, Monk J. Strain-driven grain boundary motion in nanocrystalline materials. *Mater Sci Eng, A* 2008;493(1–2):33–40.
- [39] Liu Z, Li P, Xiong L, Liu T, He L. High-temperature tensile deformation behavior and microstructure evolution of Ti55 titanium alloy. *Mater Sci Eng, A* 2017;680:259–69.
- [40] Jain V, Mishra RS. Superplastic behavior and microstructural stability of friction stir processed AZ91C alloy. *J Mater Sci* 2013;48(6):2635–46.
- [41] Kaibyshev OA. Superplasticity of alloys, intermetallics and ceramics. Springer Science & Business Media; 2012.
- [42] Jeong HG, Jeong YG, Kim WJ. Microstructure and superplasticity of AZ31 sheet fabricated by differential speed rolling. *J Alloys Compd* 2009;483(1–2):279–82.
- [43] Watanabe H, Kurimoto K, Uesugi T, Takigawa Y, Higashi K. Isotropic superplastic flow in textured magnesium alloy. *Mater Sci Eng, A* 2012;558:656–62.
- [44] Momeni A, Ebrahimi GR, Jahazi M, Bocher P. Microstructure evolution at the onset of discontinuous dynamic recrystallization: a physics-based model of subgrain critical size. *J Alloys Compd* 2014;587:199–210.
- [45] Abu-Farha F, Nazzal M, Curtis R. Optimum specimen geometry for accurate tensile testing of superplastic metallic materials. *Exp Mech* 2011;51(6):903–17.
- [46] Park CH, Ko YG, Park JW, Lee CS. Enhanced superplasticity utilizing dynamic globalization of Ti–6Al–4V alloy. *Mater Sci Eng, A* 2008;496(1–2):150–8.
- [47] Zhang W, Ding H, Pereira PHR, Huang Y, Langdon TG. Grain refinement and superplastic flow in a fully lamellar Ti–6Al–4V alloy processed by high-pressure torsion. *Mater Sci Eng, A* 2018;732:398–405.
- [48] Jiang YQ, Lin YC, Jiang XY, He DG, Zhang XY, Kotkunde N. Hot tensile properties, microstructure evolution and fracture mechanisms of Ti–6Al–4V alloy with initial coarse equiaxed phases. *Mater Char* 2020;163:110272.
- [49] Lin YC, Wu Q, Pang GD, Jiang XY, He DG. Hot tensile deformation mechanism and dynamic softening behavior of Ti–6Al–4V alloy with thick lamellar microstructures. *Adv Eng Mater* 2020;22(3):1901193.
- [50] Hémery S, Villechaise P. In situ EBSD investigation of deformation processes and strain partitioning in bi-modal Ti–6Al–4V using lattice rotations. *Acta Mater* 2019;171:261–74.